ACS Catalysis
Research Article
pubs.acs.org/acscatalysis

Effects of Surface Defects on Photocatalytic H_2O_2 Production by Mesoporous Graphitic Carbon Nitride under Visible Light Irradiation

Yasuhiro Shiraishi,*[†,‡] Yusuke Kofuji,[†] Hirokatsu Sakamoto,[†] Shunsuke Tanaka,[§] Satoshi Ichikawa,[⊥] and Takayuki Hirai[†]

[†]Research Center for Solar Energy Chemistry, and Division of Chemical Engineering, Graduate School of Engineering Science, Osaka University, Toyonaka 560-8531, Japan

[‡]PRESTO, JST, Saitama 332-0012, Japan

[§]Department of Chemical, Energy and Environmental Engineering, Kansai University, Suita 564-8680, Japan

[⊥]Institute for NanoScience Design, Osaka University, Toyonaka 560-8531, Japan

Supporting Information

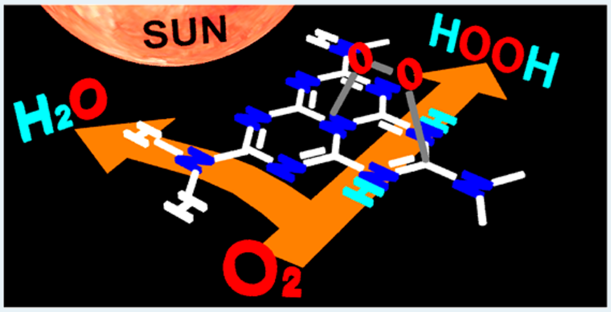

ABSTRACT: Photocatalytic production of hydrogen peroxide (H_2O_2) from ethanol (EtOH) and molecular oxygen (O_2) was carried out by visible light irradiation ($\lambda > 420$ nm) of mesoporous graphitic carbon nitride (GCN) catalysts with different surface areas prepared by silica-templated thermal polymerization of cyanamide. On these catalysts, the photoformed positive hole oxidize EtOH and the conduction band electrons localized at the 1,4-positions of the melem unit promote two-electron reduction of O_2 (H_2O_2 formation). The GCN catalysts with 56 and 160 $m^2\ g^{-1}$ surface areas exhibit higher activity for H_2O_2 production than the catalyst prepared without silica template (surface area: 10 $m^2\ g^{-1}$), but a further increase in the surface area (228 $m^2\ g^{-1}$) decreases the activity. In addition, the selectivity for H_2O_2 formation significantly decreases with an increase in the surface area. The mesoporous GCN with larger surface areas inherently contain a larger number of primary amine moieties at the surface of mesopores. These defects behave as the active sites for four-electron reduction of O_2, thus decreasing the H_2O_2 selectivity. Furthermore, these defects also behave as the active sites for photocatalytic decomposition of the formed H_2O_2. Consequently, the GCN catalysts with relatively large surface area but with a small number of surface defects promote relatively efficient H_2O_2 formation.

KEYWORDS: *photocatalysis, hydrogen peroxide, graphitic carbon nitride, visible light, oxygen reduction*

INTRODUCTION

Hydrogen peroxide (H_2O_2) is a versatile clean oxidant that emits only water as a byproduct and is widely used for pulp bleaching, disinfection, and organic synthesis.[1] H_2O_2 has also attracted much attention as a new energy carrier for fuel cells, alternative to H_2, because it is water-soluble and can be used in an one-compartment cell for electricity generation.[2] H_2O_2 is currently manufactured in industry by the anthraquinone method that needs high-energy-consuming two-step oxidation and hydrogenation reactions on Pd-based catalysts.[3] Recently, H_2O_2 synthesis with H_2 and O_2 has been studied extensively with Pd[4] or Au−Pd bimetallic catalysts.[5] This direct synthesis quantitatively produces H_2O_2 but requires extreme care because of the potentially explosive nature of the H_2/O_2 mixed gases. A new catalytic process capable of producing H_2O_2 without H_2 is therefore desired.

Photocatalytic H_2O_2 production on semiconductor catalysts such as titanium dioxide (TiO_2) has also been studied.[6−8] The reactions are carried out by UV irradiation ($\lambda < 400$ nm) of O_2-saturated water with a catalyst in the presence of an electron and proton donor, such as alcohols. Photoexcitation of the catalyst produces the positive hole (h^+) and electron (e^-) pairs. The h^+ oxidize alcohol and produce aldehyde and H^+ (eq 1), while the e^- promote two-electron reduction of O_2 and produce H_2O_2 (eq 2).

$$R{-}CH_2OH + 2h^+ \rightarrow R{-}CHO + 2H^+ \qquad (1)$$

$$O_2 + 2H^+ + 2e^- \rightarrow H_2O_2 \qquad (2)$$

The reaction proceeds at ambient temperature without H_2 and is potentially a safe and sustainable H_2O_2 synthesis. Its efficiency is, however, very low because the selectivity for the amount of H_2O_2 formed relative to the amount of alcohol consumed is ~6%.[9−11] This is because one-electron reduction of O_2 (superoxide ($^{\bullet}OOH$) radical formation, eq 3) and four-electron reduction of O_2 (water formation, eq 4) occur

Received: February 25, 2015
Revised: April 9, 2015
Published: April 9, 2015

DOI: 10.1021/acscatal.5b00408
ACS Catal. 2015, 5, 3058−3066

predominantly on the catalysts. These suppress two-electron reduction of O_2 (eq 2), resulting in very low H_2O_2 selectivity.

$$O_2 + H^+ + e^- \rightarrow {}^{\bullet}OOH \tag{3}$$

$$O_2 + 4H^+ + 4e^- \rightarrow 2H_2O \tag{4}$$

Earlier, we found that graphitic carbon nitride (GCN), a metal-free polymeric semiconductor with a graphitic stacking structure of melem sheets,[12,13] promotes selective two-electron reduction of O_2 and efficiently produces H_2O_2.[14,15] Visible light irradiation ($\lambda > 420$ nm) of GCN with a small surface area 10 $m^2\ g^{-1}$ (GCN(10) catalyst), prepared by a simple thermal polymerization of cyanamide,[12] produces H_2O_2 with ~90% selectivity. Raman spectroscopy, electron spin resonance (ESR), and ab initio calculation revealed that the selective two-electron reduction of O_2 is ascribed to the efficient formation of 1,4-endoperoxide species on the melem unit. As shown in Scheme 1, the photoformed e^- are localized at the 1,4-positions of the melem unit (a). The e^- reduces O_2 and creates a superoxo radical (b). This is rapidly reduced by another e^- at the para position and produces the 1,4-endoperoxide species (c), which is readily transformed to H_2O_2. The efficient formation of 1,4-endoperoxide (b → c) may suppresses one-electron reduction of O_2 (${}^{\bullet}OOH$ formation, eq 3) and four-electron reduction of O_2 (water formation, eq 4), thus promoting selective two-electron reduction of O_2 (eq 2).

Scheme 1. Proposed Mechanism for Selective Formation of H_2O_2 on the Photoactivated GCN Surface

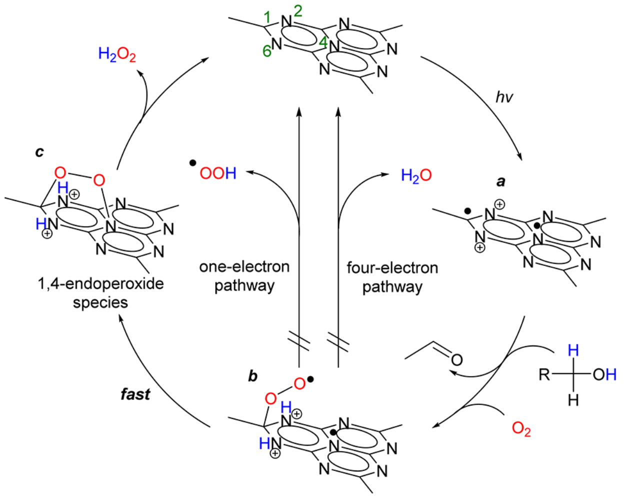

The purpose of the present work is to improve the catalytic activity of GCN while maintaining high H_2O_2 selectivity. It is well-known that the photocatalytic activity of semiconductor materials increases with an increase in their surface area.[16−18] Some postsynthesis methods for the surface area enlargement of GCN have been proposed, such as exfoliation of melem sheets by thermal oxidation etching,[19] ultrasonication,[20,21] and scission of the parts of the C−N bonds by chemical or thermal treatments.[22,23] A more popular way is the direct synthesis of GCN with large surface areas. Several methods have been proposed, such as creation of mesoporous GCN by thermal polymerization of different C, N-containing precursors, such as urea, thiourea, and guanidine derivatives,[24−26] and creation of GCN nanowires, nanorods, or nanofibers by the treatment of melamine with HNO_3 followed by thermal polymerization.[27−29] The most simple and widely accepted method is the creation of mesoporous GCN based on the silica-templating method reported by Wang et al.[30,31] They synthesized mesoporous GCN by thermal polymerization of cyanamide with silica particles (~12 nm) as a template, followed by removal of the particles by washing with base. This produces mesoporous GCN with a very large surface area (up to 380 $m^2\ g^{-1}$), which can easily be controlled by the amount of silica particles added. Several accounts in the literature have revealed that a variety of photoreactions, such as H_2 evolution,[30,31] alcohol oxidation,[32] CO_2 reduction,[33] radical polymerization,[34] air purification,[22] and pollutant degradation,[35] proceed efficiently on the mesoporous GCN with increased surface areas as compared with the nonporous GCN.

In the present work, we synthesized GCN(x) catalysts with different surfaces areas (x ($m^2\ g^{-1}$) = 56, 160, and 228) by the silica-templated polymerization of cyanamide[30,31] and used them for photocatalytic H_2O_2 production with ethanol (EtOH) as an electron and proton donor under visible light irradiation ($\lambda > 420$ nm). A similar photocatalytic system for alcohol oxidation on mesoporous GCN has already been reported by another group;[32] however, there is no mention of H_2O_2 formation. In the present study, photocatalytic activity for "EtOH oxidation" increases with an increase in the surface area of the catalysts, as reported.[32] We found that GCN(56) and (160) catalysts exhibit higher activity for "H_2O_2 formation" than nonporous GCN(10), but GCN(228) shows decreased activity. In addition, the selectivity for H_2O_2 formation significantly decreases on the catalysts with larger surface areas. ESR, X-ray photoelectron spectroscopy (XPS), electrochemical analysis, and ab initio calculation have revealed that the catalysts with larger surface areas contain a larger number of primary amine moieties at the surface of the mesopores. These surface defects behave as active sites for four-electron reduction of O_2 (eq 4), thus decreasing the H_2O_2 selectivity. In addition,

Table 1. Properties of the Respective Catalysts

catalyst	S_{BET}[a], $m^2\ g^{-1}$	D_p[b], nm	V_p[c], $cm^3\ g^{-1}$	E_{bg}[d], eV	composition of N atoms[e], %				
					$N_{pyridine}$	N_{center}	$N_{tertiary}$	$N_{secondary}$	$N_{primary}$
GCN(10)	10			2.62	71.6	11.9	13.9	2.0	0.6
GCN(56)	56	15.4	0.18	2.61	70.3	11.7	12.2	3.9	1.9
GCN(160)	160	11.2	0.39	2.57	70.1	11.7	9.1	6.5	2.6
GCN(228)	228	9.9	0.54	2.59	70.7	11.8	5.4	8.1	4.0

[a] Brunauer−Emmett−Teller (BET) surface area. [b] Barrett−Joyner−Halenda (BJH) adsorption pore size. [c] BJH adsorption pore volume. [d] Band gap energies determined by a plot of the Kubelka−Munk function versus the energy of light absorbed (Figure S3, Supporting Information). [e] Determined by integration of N 1s XPS charts (Figure 3) and CO_2-TPD profiles (Figure 4).

these defects also behave as active sites for reductive decomposition of the formed H_2O_2. Consequently, a GCN catalyst with a relatively large surface area but with a small number of surface defects promotes relatively efficient H_2O_2 formation.

RESULTS AND DISCUSSION

Preparation and Characterization of Catalysts. Nonporous GCN(10) catalyst was obtained by calcination of cyanamide at 823 K for 4 h under N_2 as yellow powders.[12] The respective mesoporous GCN(56), (160), and (228) catalysts were prepared according to the literature procedure:[30] calcination of a mixture of cyanamide and different amounts of a Ludox HS40 solution containing ∼12 nm silica particles under N_2 at 823 K for 4 h, followed by washing with a 4 M NH_4HF_2 solution at 298 K for 24 h produced yellow powders of the catalysts.

Table 1 shows the properties of GCN catalysts. As shown in Figure S1 (Supporting Information), N_2 adsorption/desorption analysis of mesoporous GCN shows a typical type-IV isotherm, although nonporous GCN(10) shows almost no hysteresis loop. As shown in Figure 1, transmission electron microscopy (TEM) images of GCN(228) clearly exhibit mesopores, indicating that the silica-templated polymerization indeed creates a mesosphere pore structure.[13,30] As shown in Figure S2 (Supporting Information), X-ray diffraction (XRD) patterns of the catalysts shows distinctive diffraction at $2\theta = 27.4$ (d = 0.325 nm), assigned to the (002) packing of melem sheets.[12,13] In that, mesoporous GCN show a lower peak intensity than the nonporous GCN(10) because of their low crystallinity by the polymerization with a silica template, as observed in the related system.[36] Figure S3 (Supporting Information) shows the diffuse reflectance UV−vis spectra of the catalysts. Mesoporous GCN show spectra similar to those of nonporous GCN at λ >420 nm, but show stronger absorption at λ <420 nm due to the multiple light scattering effects by the mesoporous structure.[30,37] A Tauc plot of the absorption data revealed that the band gap energies of mesoporous GCN are very similar to those of the nonporous GCN (∼2.57−2.62 eV), regardless of the presence of mesopores.

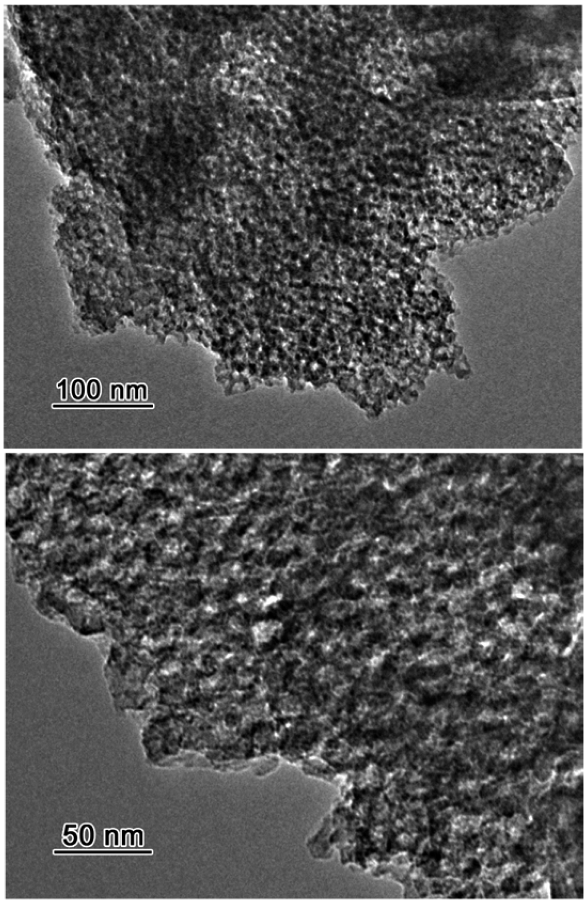

Figure 1. Typical TEM images of the GCN(228) catalyst.

Photocatalytic Activity. Photocatalytic H_2O_2 production was carried out with EtOH as the electron and proton donor.[14] An EtOH/water (9/1 v/v) mixture (5 mL) containing each respective catalyst (20 mg) was photoirradiated at λ > 420 nm by a Xe lamp with magnetic stirring under O_2 (1 atm) at 298 K. All of the systems produce CH_3CHO as the main oxidation product of EtOH with only minor amounts of CH_3COOH and CO_2, as is the case for nonporous GCN(10).[14] Figure 2a shows the time-dependent change in the amount of CH_3CHO during photoreaction on the respective catalysts. The GCN catalysts with larger surface areas exhibit a higher activity for CH_3CHO formation, indicating that, as reported in the literature,[30−35] an enlarged surface area of GCN indeed enhances photocatalytic cycles.

Figure 2b shows the time profiles for H_2O_2 formation during the reaction. GCN(56) and (160) catalysts exhibit a higher activity for H_2O_2 formation than GCN(10), but GCN(228) is ineffective. Figure 2c shows the time profiles for the selectivity of the amount of H_2O_2 formed relative to the amounts of oxidation products of EtOH $\{= [H_2O_2]/[CH_3CHO + CH_3COOH + (CO_2)/2] \times 100\}$. In the case of GCN(10), as we reported earlier,[14] the H_2O_2 selectivity at the early stage of reaction (3 h) is 92% and scarcely changes, even after prolonged photoirradiation (∼24 h). In contrast, the H_2O_2 selectivities on mesoporous GCN at 3 h are much lower and decrease with an increase in the surface area: 92% for GCN(10) > 72% for GCN(56) > 58% for GCN(160) > 42% for GCN(228). This clearly indicates that the selectivity for two-electron reduction of O_2 decreases with an increase in the surface area of catalysts.

Surface Defects on the Catalysts. The decrease in the H_2O_2 selectivity associated with an increase in the surface area of catalysts (Figure 2c) is ascribed to the formation of a large number of primary amine moieties on the surface of mesopores. As schematically shown in Scheme 2a, this originates from the polymerization of cyanamide at the silica surface. An acidic silica surface attracts the amine moieties of cyanamide molecules.[38] Thermal polymerization therefore creates primary amine moieties on the surface. Subsequent removal of silica by the dissolution with NH_4HF_2 therefore left these moieties on the surface of mesopores. These surface defects behave as the active sites for four-electron reduction of O_2 (water formation, eq 4) and, hence, decrease the selectivity for two-electron reduction of O_2 on the 1,4-positions of melem units (H_2O_2 formation, eq 2).

The formation of surface defects on the mesoporous GCN is confirmed by XPS analysis. Figure 3 shows the XPS charts for the N 1s level of the respective GCN catalysts. All of the charts can be deconvoluted into the three components. As reported[39] and as shown in Scheme 2b, these components are assigned to sp^2-hybridized N atoms of the melem units ($N_{pyridine}$) at 398.7

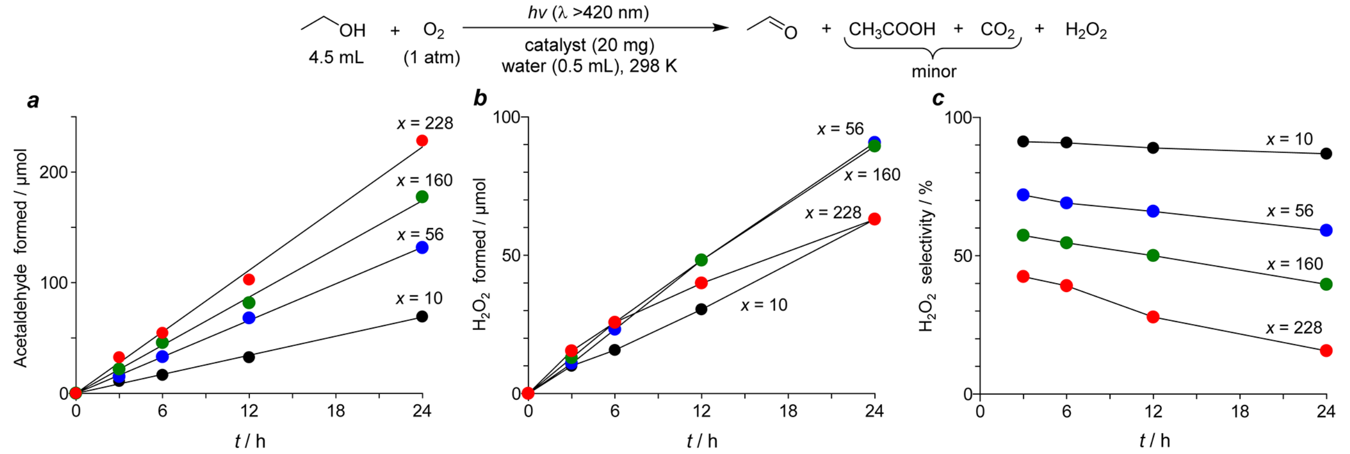

Figure 2. Time-dependent change in the amounts of (a) CH_3CHO and (b) H_2O_2 and (c) H_2O_2 selectivity during photoreaction on the respective GCN(x) catalysts. Photoirradiation was carried out with a 2 kW Xe lamp (light intensity at 420−500 nm was 26.9 W m^{-2}). H_2O_2 selectivity (%) = $[H_2O_2]/([CH_3CHO] + [CH_3COOH] + [CO_2]/2) \times 100$.

Scheme 2[a]

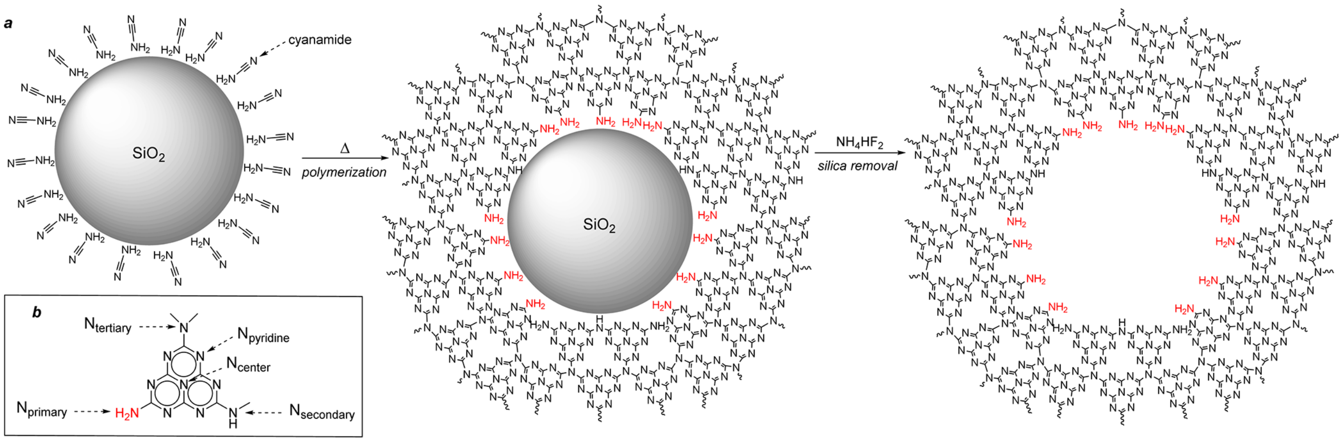

[a](a) Proposed mechanism for the formation of surface defects on the walls of mesopores. (b) Different N atoms on GCN.

eV (pink), trigonal N atoms of the melem center (N_{center}), and tertiary amine N atoms ($N_{tertiary}$) of the melem terminal at 400.2 eV (blue), and primary ($N_{primary}$) and secondary amine ($N_{secondary}$) N atoms of the melem terminal at 401.3 eV (green). The respective charts clearly show that the contribution of the green component ($N_{primary}$ + $N_{secondary}$) increases with an increase in the surface area of the catalysts. This suggests that, as shown in Scheme 2a, thermal polymerization of cyanamide in the presence of silica particles indeed creates a large number of primary and secondary amine moieties.

The formation of a large number of primary amine moieties on the GCN catalysts with larger surface areas is confirmed by temperature-programmed desorption (TPD) analysis with CO_2. Figure 4 shows the CO_2-TPD profiles for the respective catalysts. All of the profiles can be deconvoluted into three desorption peaks, assigned to the CO_2 molecules desorbed from $N_{pyridine}$ (174 °C, pink), $N_{secondary}$ (224 °C, cyan), and $N_{primary}$ sites (301 °C, purple), respectively.[40] The amount of CO_2 desorbed from the $N_{primary}$ sites increases with an increase in the surface area of the catalysts. This indicates that a GCN with larger surface areas indeed possesses a larger number of $N_{primary}$ sites. The composition of the respective N atoms on the GCN catalysts (Scheme 2b) can be determined by the integration of the deconvoluted components on the XPS (Figure 3) and CO_2-TPD data (Figure 4) and are summarized in Table 1. The composition of the primary amine moieties ($N_{primary}$) on the nonporous GCN(10) is only 0.6%, but the mesoporous GCN with larger surface areas have a larger number of $N_{primary}$ (up to 4% for GCN(228)). The results indicate that, as shown in Scheme 2a, primary amine moieties are indeed produced on the surface of mesoporous GCN catalysts.

Properties of One-Electron Reduction of O_2. The lower H_2O_2 selectivity on the mesoporous GCN is because they promote four-electron reduction of O_2 (water formation, as eq 4). One-electron reduction of O_2 ($^\bullet$OOH radical formation, eq 3) is not involved in the selectivity decrease. This is confirmed by ESR analysis with 5,5-dimethyl-1-pyrroline N-oxide (DMPO) as a spin-trapping reagent. An EtOH/water (v/v 9/1) mixture (5 mL) was photoirradiated with the respective GCN catalysts (20 mg) and DMPO (0.1 mmol). Figure 5 shows the ESR spectra of the solutions recovered after photoreaction for 3 min. All of the solutions exhibit distinctive signals assigned to the DMPO−$^\bullet$OOH spin adduct (α_N = 13.5 G; $\alpha_H{}^\beta$ = 9.8 G, g = 2.0067).[14,41] The signal intensities on the respective catalysts are very similar, indicating that similar numbers of $^\bullet$OOH radicals are produced on these catalysts. The results suggest that one-electron reduction of O_2 (eq 3) is

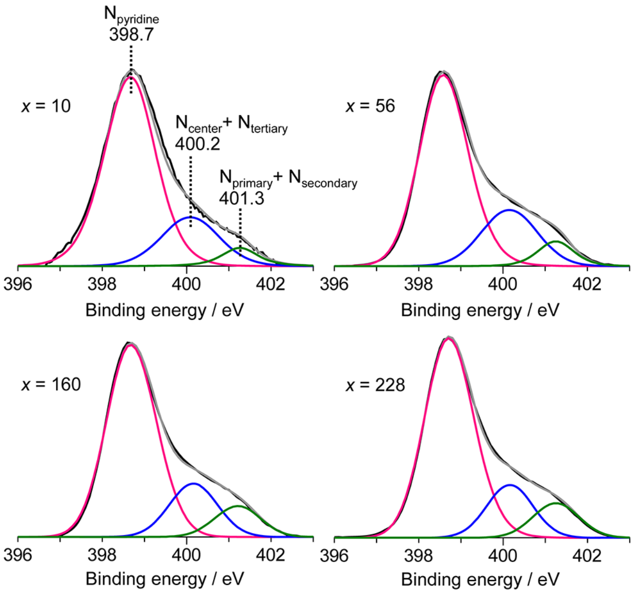

Figure 3. XPS charts for N 1s levels of GCN(x) catalysts. Black line is the obtained chart, and gray line is the sum of the deconvoluted components. The respective components are represented in Scheme 2b.

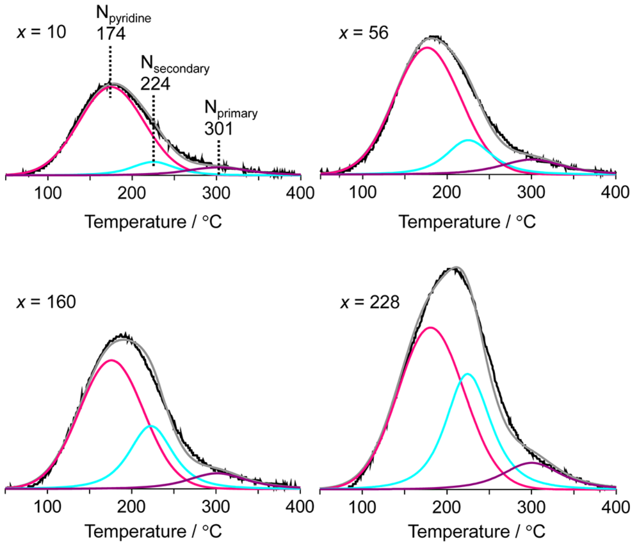

Figure 4. CO_2-TPD profiles for the respective GCN(x) catalysts. Black line is the obtained profile, and the gray line is sum of the deconvoluted components. The respective components are represented in Scheme 2b.

not involved in the decreased H_2O_2 selectivity on the mesoporous GCN catalysts.

Properties of Four-Electron Reduction of O_2. The lower H_2O_2 selectivity on mesoporous GCN is ascribed to the enhanced four-electron reduction of O_2. Electrochemical analysis with a rotating disk electrode confirms this. Figure 6a shows the linear sweep voltammograms of GCN(10) and (228) catalysts measured on a rotating disk electrode in a buffered aqueous solution (pH 7) under O_2 atmosphere at different rotating speeds.[42,43] The diagnostic Koutecky−Levich plots of the data obtained at a constant electrode potential (−0.4 V) are illustrated in Figure 6b, and the slope of the plots obtained by linear regression was used to estimate the average number of electrons (n) involved in the overall reduction of O_2.[44,45] The plots were interpreted on the following equations, where j is the

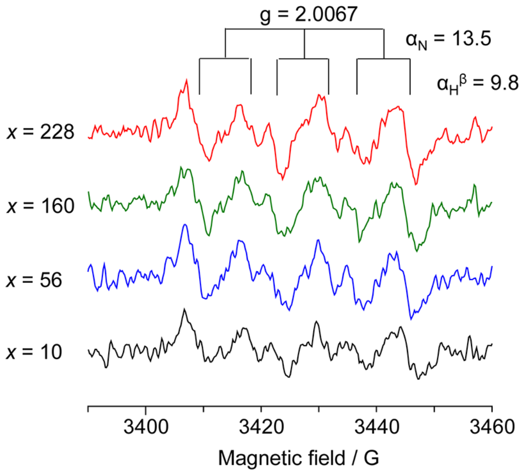

Figure 5. ESR spectra measured at 298 K for the solutions recovered after photoirradiation of the respective GCN(x) catalysts in an EtOH/water/O_2 system. Photoirradiation was performed for 3 min under conditions identical to those in Figure 2 with DMPO (0.1 mmol).

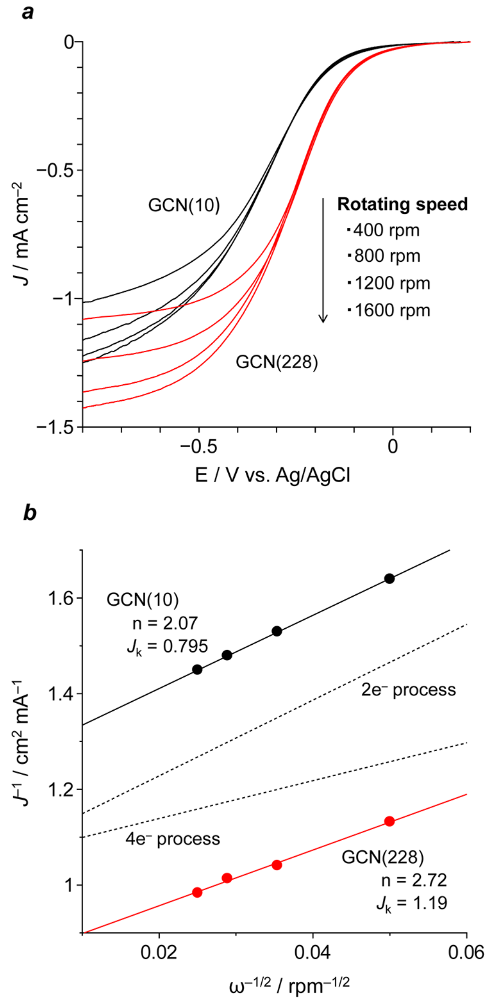

Figure 6. (a) Linear-sweep voltammograms of GCN(10) and GCN (228) catalysts measured on a rotating disk electrode at different rotating speeds. (b) The Koutecky−Levich plots of the data obtained at the constant electrode potential (−0.4 V).

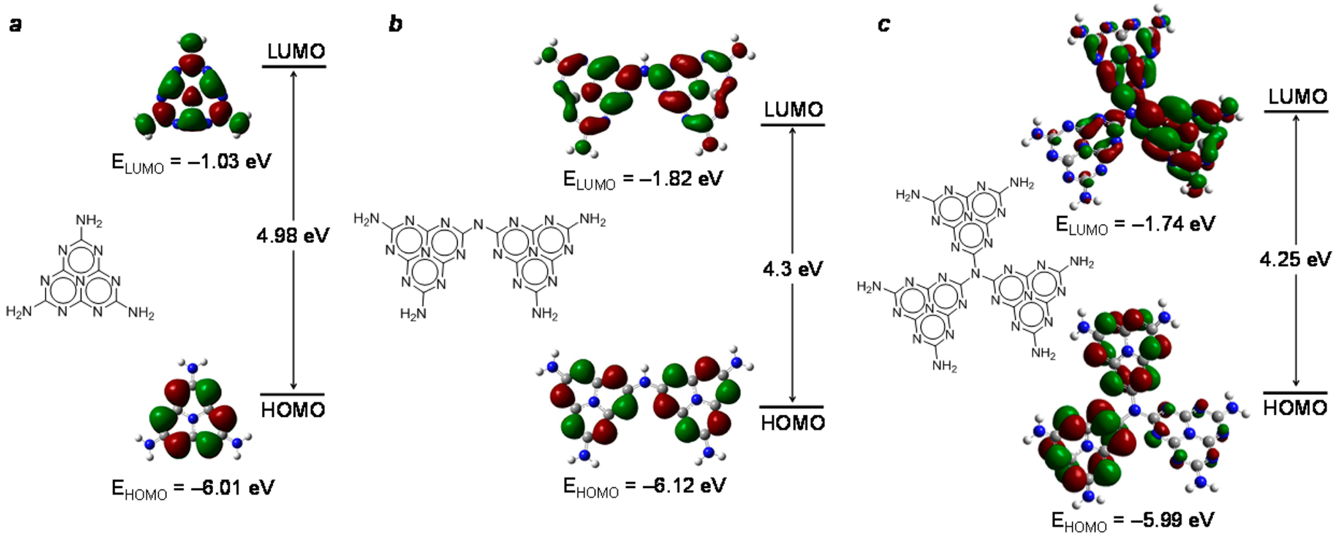

Figure 7. Interfacial plots of main orbitals for (a) single, (b) double, and (c) triple melem-conjugated models, calculated at the DFT level (B3LYP/6-31G(d)).

measured current density, j_k is the kinetic current density, and ω is the electrode rotating speed (rpm), respectively:

$$j^{-1} = j_k^{-1} + B^{-1}\omega^{-1/2} \tag{5}$$

$$B = 0.2nF\nu^{-1/6}CD^{2/3} \tag{6}$$

F is the Faraday constant (96 485 C mol^{-1}), ν is the kinetic viscosity of water (0.01 $\text{cm}^2\ \text{s}^{-1}$), C is the bulk concentration of O_2 in solution (1.3×10^{-6} mol cm^{-3}), and D is the diffusion coefficient of O_2 (2.7×10^{-5} $\text{cm}^2\ \text{s}^{-1}$), respectively.[46] The j_k values obtained on the GCN(10) and GCN(228) catalysts determined by the intercept of the Koutecky−Levich plots are 0.79 and 1.19 mA cm^{-2}, respectively. The larger j_k value of GCN(228) indicates that O_2 is reduced more efficiently because of the larger surface area.[47] The n value for GCN(10), determined by the slope, is 2.07, indicating that the GCN catalyst with a small surface area indeed selectively promotes two-electron reduction of O_2 (n = 2).[48] This is consistent with high H_2O_2 selectivity (∼90%) obtained by photoreaction experiments (Figure 2c). In contrast, the n value for GCN(228) is 2.72, which is much larger than that of GCN(10). This indicates that the GCN catalyst with a larger surface area indeed promotes four-electron reduction of O_2 (n = 4). This is also consistent with the decreased H_2O_2 selectivity during photoreaction (Figure 2c).

Recently, Zheng et al.[49] performed electrochemical analysis for O_2 reduction on the mesoporous GCN with a large surface area (250 $\text{m}^2\ \text{g}^{-1}$), prepared by thermal polymerization of cyanamide in the presence of a SBA-15 mesoporous silica as a template, followed by the removal of template by washing with NH_4HF_2. This material also exhibits a large n value (2.6), similar to that obtained in the present study. This supports the enhanced four-electron reduction of O_2 on GCN with a large surface area. The change in multielectron reduction properties of O_2 is associated reasonably well with an increase in the number of primary amine moieties (N_{primary}) on the GCN catalysts. These findings therefore imply that these defects sites may contribute to the enhanced four-electron reduction of O_2.

Photoreduction Properties of the Surface Defects. As shown in Scheme 1, the conduction band electrons formed on the nonporous GCN catalyst with a small surface area are localized at the 1,4-positions of the melem unit. They reduce O_2 and rapidly produce 1,4-endoperoxide species, which is readily transformed to H_2O_2. This thus promotes selective two-electron reduction of O_2.[14] In contrast, on the mesoporous GCN catalysts with a larger surface areas, a large number of primary amine moieties on the melem terminal behave as the active sites for four-electron reduction of O_2. This results in decreased H_2O_2 selectivity. This is confirmed by ab initio calculations of the conjugated melem models (Figure 7) based on the time-dependent density functional theory (TD-DFT), performed within the Gaussian03 program. The electronic transitions of all of the single, double, and triple melem models are mainly contributed by HOMO → LUMO ($S_0 \rightarrow S_1$) transitions. Interfacial plots for the respective orbitals are summarized in Figure 7. The electrons on HOMO for the double and triple melem models are located at the 2,6-positions of the melem unit. This suggests that these nitrogen atoms on the melem units behave as the oxidation sites, as is the case for the single melem model.[15]

In the case of the single melem model (a), as we reported earlier,[15] the LUMO electrons are located at the 1,4-positions of the melem. This suggests that the conduction band electrons are, indeed, localized on these atoms, and they behave as the sites for two-electron reduction of O_2. In this case, LUMO electrons are also located at the terminal primary amine moiety. This indicates that conduction band electrons are also localized on these sites, and they also behave as the reduction sites. In the case of the double melem model (b), LUMO electrons are also located at the 1,4-positions of melem and the terminal primary amine moieties. In this case, the secondary amine moiety situated between two melem moieties does not possess an electron distribution. This suggests that the secondary amine moiety does not act as the reduction sites. In the case of the triple melem model (c), the LUMO electrons are also not located at the tertiary amine moiety. The above facts involving (i) a large distribution of LUMO electrons onto the primary amine moieties and (ii) the decrease in H_2O_2 selectivity with an increase in the amount of primary amine moiety strongly suggest that the primary amine moieties on the surface of mesopores behave as the active sites for four-electron reduction of O_2. As a result of this, GCN catalysts with a larger surface area exhibit decreased H_2O_2 selectivity.

Photocatalytic Decomposition of H_2O_2. As shown in Figure 2c, during the photocatalytic H_2O_2 production, the H_2O_2 selectivity obtained on the GCN(10) catalyst scarcely changes, even after prolonged irradiation (∼90%). In contrast, the H_2O_2 selectivity on the mesoporous GCN catalysts decreases with the irradiation time, and the decrease is more apparent for the catalysts with the larger surface areas. The results clearly indicate that the mesoporous GCN with the larger surface areas promote subsequent decomposition of the formed H_2O_2. Stirring the H_2O_2 solutions with respective catalysts in the dark or under photoirradiation without catalyst under N_2 atmosphere scarcely changes the H_2O_2 amount. This suggests that H_2O_2 is photocatalytically decomposed on the mesoporous GCN. As reported for several semiconductor photocatalytic systems,[44,50] H_2O_2 is reductively decomposed by the donation of conduction band electrons as follows:

$$H_2O_2 + 2H^+ + 2e^- \rightarrow 2H_2O \tag{7}$$

The GCN(10) catalyst (20 mg) was added to an EtOH/water mixture (9/1 v/v, 5 mL) with 200 μmol H_2O_2 and photoirradiated ($\lambda > 420$ nm) under N_2 atmosphere. As shown in Figure S4 (Supporting Information), photoirradiation leads to a decrease in the H_2O_2 amount. As shown in Table 1, the GCN(10) catalyst contains a very small amount of the primary amine moieties. This indicates that the 1,4-positions of the melem unit behave as the active sites for photocatalytic decomposition of H_2O_2 (eq 7). However, as shown in Figure 2c, H_2O_2 selectivity on the GCN(10) catalyst scarcely changes, even after prolonged photoirradiation. This means that, during photoirradiation with O_2, the 1,4-positions of the melem units predominantly reduce O_2 and scarcely decompose H_2O_2. The significant decrease in the H_2O_2 selectivity with time on the mesoporous GCN catalysts is therefore probably due to the photocatalytic decomposition of H_2O_2 on the primary amine moieties. On these sites, basic primary amine moieties[51,52] attract the acidic H_2O_2 molecules. This may promote rapid H_2O_2 decomposition on the mesoporous GCN catalysts with larger surface areas.

CONCLUSION

Mesoporous GCN prepared by thermal polymerization of cyanamide with silica nanoparticles as a template followed by removal of the particles was used for photocatalytic H_2O_2 production from EtOH and O_2 in water under irradiation of visible light. The GCN catalysts with larger surface areas inherently contain a larger number of primary amine moieties on the surface of mesopores. Selectivity for H_2O_2 formation via two-electron reduction of O_2 by the conduction band electrons localized on the 1,4-positions of the melem unit decreases with an increase in the surface area. This is because the primary amine moieties behave as the active sites for four-electron reduction of O_2. These basic primary amine sites also behave as the sites for reductive decomposition of the formed H_2O_2, probably due to the strong interaction with acidic H_2O_2. The obtained results suggest that creation of GCN catalysts with a large surface area but with a smaller number of primary amine moieties is very important for efficient photocatalytic H_2O_2 production.

EXPERIMENTAL SECTION

GCN(10). Cyanamide (9.0 g) was added to a porcelain cup and calcined under N_2 flow at 823 K for 4 h with the heating rate being 2.3 K min^{-1}. Grinding of the resultant gave yellow powders of GCN(10).

GCN(*x*) (*x* = 56, 160, and 228). Cyanamide (3.0 g) was mixed with different amounts of a Ludox HS40 solution (40% solution of ∼12 nm silica particles; 3.6, 7.5, and 11.3 g, respectively) and stirred at 333 K for 12 h. The resultant was calcined under N_2 flow at 823 K for 4 h, with the heating rate being 2.3 K min^{-1}. The resulting powders were stirred in a NH_4HF_2 solution (4 M) at 298 K for 24 h to remove the silica template particles. The obtained powders were recovered by centrifugation and washed thoroughly with water until the pH of the solution became ∼7.0. They were then washed with EtOH and dried at 343 K in vacuo for 12 h.

Photoreaction. Each respective catalyst (20 mg) was added to an EtOH/water mixture (9/1 v/v, 5 mL) within a Pyrex glass tube (φ 12 mm; capacity, 20 mL), and the tube was sealed with a rubber septum cap. The catalyst was dispersed well by ultrasonication for 5 min, and O_2 was bubbled through the solution for 5 min. The respective tube was immersed in a temperature-controlled water bath (298 ± 0.5 K)[53] and photoirradiated with magnetic stirring using a 2 kW Xe lamp (USHIO Inc.).[54] A 20 wt % $NaNO_2$ solution was used as a filter to give light wavelengths at $\lambda > 420$ nm.[55] The light intensity at 420−500 nm was determined to be 26.9 W m^{-2}. After the photoreaction, the gas-phase products were analyzed by GC-TCD (Shimadzu, GC-8A). The catalyst was then recovered by centrifugation. The H_2O_2 amount in the resulting solution was determined by a redox titration with $KMnO_4$. Other liquid-phase products were quantified by GC−FID (Shimadzu, GC-2010).

ESR Analysis. The spectra were recorded at the X band using a Bruker EMX-10/12 spectrometer with a 100 kHz magnetic field modulation at a microwave power level of 10.5 mW, where microwave power saturation of the signals does not occur.[56] The magnetic field was calibrated with a 1,1′-diphenyl-2-picrylhydrazyl (DPPH) as a standard. The measurements were carried out as follows: catalyst (20 mg) was suspended in an EtOH/water mixture (9/1 v/v, 5 mL) containing DMPO (0.1 mmol) within a Pyrex glass tube (φ = 12 mm; capacity, 20 mL), and the tube was sealed with a rubber septum cap. After ultrasonication (3 min) and O_2 bubbling (5 min), the tube was photoirradiated at $\lambda > 420$ nm with magnetic stirring for 3 min. After the photoirradiation, the catalyst was recovered by centrifugation, and the resulting solution was subjected to ESR analysis.

Electrochemical Analysis. The rotating disk electrode analysis was performed on a computer-controlled CHI600D advanced electrochemical system with a three-electrode cell. A Ag/AgCl electrode and a Pt wire electrode were used as the reference and counter electrodes, respectively.[47,49] The working electrode was prepared according to the procedure described in literature:[49] the respective GCN catalysts (20 mg) were dispersed in water (5 mL) by ultrasonication. The suspension (20 μL) was put onto a Pt disk electrode and dried at room temperature. Linear sweep voltammograms were obtained in an O_2-saturated 0.1 M phosphate buffer solution (pH 7) with a scan rate of 10 mV s^{-1} at different rotating speeds (400−1600 rpm). After each scan, O_2 was bubbled through the electrolyte for 5 min to saturate O_2.

Calculation Details. All of the calculations were performed with tight convergence criteria at the DFT level with the Gaussian03 package, using the B3LYP/6-31G(d) basis set for all atoms. The excitation energies and the oscillator strengths were calculated by TD-DFT at the same level for optimization using the polarizable continuum model (PCM). Cartesian coordinates for the respective single, double, and triple melem-conjugated models are summarized at the end of the Supporting Information.

Other Analysis. XRD measurements were carried out on a Philips X′Pert-MPD spectrometer. Diffuse reflectance UV−vis spectra were measured on a V-550 UV−vis spectrophotometer (JASCO Corp.) equipped with an Integrated Sphere Apparatus (ISV-469) using BaSO$_4$ as a reference. XPS charts were measured on a JEOL JPS-9000MX spectrometer using Mg Kα radiation as the energy source. N$_2$ adsorption/desorption analysis and CO$_2$-TPD measurements were carried out on an AUTOSORB-1-C/TCD analyzer (Yuasa Ionics Co., Ltd.). TEM observations were performed using an FEI Tecnai G2 20ST analytical electron microscope operated at 200 kV.[57]

■ ASSOCIATED CONTENT

Supporting Information

The following file is available free of charge on the ACS Publications website at DOI: 10.1021/acscatal.5b00408.

> N$_2$ adsorption/desorption isotherms (Figure S1); XRD patterns (Figure S2); diffuse reflectance UV−vis spectra (Figure S3); results of photocatalytic decomposition of H$_2$O$_2$ (Figure S4); Cartesian coordinates for single, double, and triple melem models (PDF)

■ AUTHOR INFORMATION

Corresponding Author

*E-mail: shiraish@cheng.es.osaka-u.ac.jp.

Notes

The authors declare no competing financial interest.

■ ACKNOWLEDGMENTS

This work was supported by a Grant-in-Aid for Scientific Research (No. 26289296) from the Ministry of Education, Culture, Sports, Science and Technology, Japan (MEXT), and by the Precursory Research for Embryonic Science and Technology (PRESTO) from Japan Science and Technology Agency (JST).

■ REFERENCES

(1) Campos-Martin, J. M.; Blanco-Brieva, G.; Fierro, J. L. G. *Angew. Chem., Int. Ed.* **2006**, *45*, 6962−6984.

(2) Mousavi Shaegh, S. A.; Nugyen, N.-T.; Ehteshami, S. M. M.; Chan, S. H. *Energy Environ. Sci.* **2012**, *5*, 8225−8228.

(3) Sandelin, F.; Oinas, P.; Salmi, T.; Paloniemi, J.; Haario, H. *Ind. Eng. Chem. Res.* **2006**, *45*, 986−992.

(4) Liu, Q.; Bauer, J. C.; Schaak, R. E.; Lunsford, J. H. *Angew. Chem., Int. Ed.* **2008**, *47*, 6221−6224.

(5) Edwards, J. K.; Solsona, B.; Ntainjua, E. N.; Carley, A. F.; Herzing, A. A.; Kiely, C. J.; Hutchings, G. J. *Science* **2009**, *323*, 1037−1041.

(6) Teranishi, M.; Naya, S.; Tada, H. *J. Am. Chem. Soc.* **2010**, *132*, 7850−7851.

(7) Maurino, V.; Minero, C.; Mariella, G.; Pelizzetti, E. *Chem. Commun.* **2005**, 2627−2629.

(8) Tsukamoto, D.; Shiro, A.; Shiraishi, Y.; Sugano, Y.; Ichikawa, S.; Tanaka, S.; Hirai, T. *ACS Catal.* **2012**, *2*, 599−603.

(9) Cai, R.; Kubota, Y.; Fujishima, A. *J. Catal.* **2003**, *219*, 214−218.

(10) Goto, H.; Hanada, Y.; Ohno, T.; Matsumura, M. *J. Catal.* **2004**, *225*, 223−229.

(11) Hirakawa, T.; Nosaka, Y. *J. Phys. Chem. C* **2008**, *112*, 15818−15823.

(12) Wang, X.; Maeda, K.; Thomas, A.; Takanabe, K.; Xin, G.; Carlsson, J. M.; Domen, K.; Antonietti, M. *Nat. Mater.* **2009**, *8*, 76−80.

(13) Thomas, A.; Fischer, A.; Goettmann, F.; Antonietti, M.; Müller, J. O.; Schlögl, R.; Carlsson, J. M. *J. Mater. Chem.* **2008**, *18*, 4893−4908.

(14) Shiraishi, Y.; Kanazawa, S.; Sugano, Y.; Tsukamoto, D.; Sakamoto, H.; Ichikawa, S.; Hirai, T. *ACS Catal.* **2014**, *4*, 774−780.

(15) Shiraishi, Y.; Kanazawa, S.; Kofuji, Y.; Sakamoto, H.; Ichikawa, S.; Tanaka, S.; Hirai, T. *Angew. Chem., Int. Ed.* **2014**, *53*, 13454−13459.

(16) Wang, J.; Ma, J.; Li, X.; Li, Y.; Zhang, G.; Zhang, F.; Fan, X. *Chem. Commun.* **2014**, *50*, 14237−14240.

(17) Shiraishi, Y.; Saito, N.; Hirai, T. *J. Am. Chem. Soc.* **2005**, *127*, 12820−12822.

(18) Li, L.; Methira, K.; Sebastian, W. P.; Morgan, S.; Ulrich, W.; Ullrich, S.; Dominik, E. *Chem. Commun.* **2010**, *46*, 7620−7622.

(19) Niu, P.; Zhang, L.; Liu, G.; Cheng, H.-M. *Adv. Funct. Mater.* **2012**, *22*, 4763−4770.

(20) Zhang, X.; Xie, X.; Wang, H.; Zhang, J.; Pan, B.; Xie, Y. *J. Am. Chem. Soc.* **2013**, *135*, 18−21.

(21) Schwinghammer, K.; Mesch, M. B.; Duppel, V.; Ziegler, C.; Senker, J.; Lotsch, B. V. *J. Am. Chem. Soc.* **2014**, *136*, 1730−1733.

(22) Sano, T.; Tsutsui, S.; Koike, K.; Hirakawa, T.; Teramoto, Y.; Negishi, N.; Takeuchi, K. *J. Mater. Chem. A* **2013**, *1*, 6489−6496.

(23) Dong, F.; Wanga, Z.; Sun, Y.; Ho, W.-K.; Zhang, H. *J. Colloid Interface Sci.* **2013**, *401*, 70−79.

(24) Martin, D. J.; Qiu, K.; Shevlin, S. A.; Handoko, A. D.; Chen, X.; Guo, Z.; Tang, J. *Angew. Chem., Int. Ed.* **2014**, *53*, 9240−9245.

(25) Zhang, G.; Zhang, J.; Zhang, M.; Wang, X. *J. Mater. Chem.* **2012**, *22*, 8083−8091.

(26) Shi, L.; Liang, L.; Wang, F.; Maa, J.; Sun, J. *Catal. Sci. Technol.* **2014**, *4*, 3235−3243.

(27) Tahir, M.; Cao, C.; Butt, F. K.; Butt, S.; Idrees, F.; Mahmood, N.; Ali, Z.; Aslam, I.; Tanveer, M.; Rizwana, M.; Mahmooda, T. *J. Mater. Chem. A* **2013**, *1*, 13949−13955.

(28) Gao, J.; Zhou, Y.; Li, Z.; Yan, S.; Wang, N.; Zou, Z. *Nanoscale* **2012**, *4*, 3687−3692.

(29) Tahir, M.; Cao, C.; Butt, F. K.; Butt, S.; Idrees, F.; Ali, Z.; Aslam, I.; Tanveer, M.; Mahmoodc, A.; Mahmoodc, N. *CrystEngComm* **2014**, *16*, 1825−1830.

(30) Wang, X.; Maeda, K.; Chen, X.; Takanabe, Kazuhiro; Domen, K.; Hou, Y.; Fu, X.; Antonietti, M. *J. Am. Chem. Soc.* **2009**, *131*, 1680−1681.

(31) Chen, X.; Jun, Y.-S.; Takanabe, K.; Maeda, K.; Domen, K.; Fu, X.; Antonietti, M.; Wang, X. *Chem. Mater.* **2009**, *21*, 4093−4095.

(32) Su, F.; Mathew, S. C.; Lipner, G.; Fu, X.; Antonietti, M.; Blechert, S.; Wang, X. *J. Am. Chem. Soc.* **2010**, *132*, 16299−16301.

(33) Maeda, K.; Kuriki, R.; Zhang, M.; Wang, X.; Ishitani, O. *J. Mater. Chem. A* **2014**, *2*, 15146−15151.

(34) Kiskan, B.; Zhang, J.; Wang, X.; Antonietti, M.; Yagci, Y. *ACS Macro Lett.* **2012**, *1*, 546−549.

(35) Lee, S. C.; Lintang, H. O.; Yuliati, L. *Chem. - Asian J.* **2012**, *7*, 2139−2144.

(36) Xu, J.; Wu, H.-T.; Wang, X.; Xue, B.; Li, Y.-X.; Cao, Y. *Phys. Chem. Chem. Phys.* **2013**, *15*, 4510−4517.

(37) Li, G.; Zhang, D.; Yu, J.-C. *Chem. Mater.* **2008**, *20*, 3983−3992.

(38) Guo, C.; Holland, G. P. *J. Phys. Chem. C* **2014**, *118*, 25792−25801.

(39) Ding, Z.; Chen, X.; Antonietti, M.; Wang, X. *ChemSusChem* **2011**, *4*, 274−281.

(40) Zhu, J.; Xiao, P.; Li, H.; Carabineiro, S. A. C. *ACS Appl. Mater. Interfaces* **2014**, *6*, 16449−16465.

(41) Harbour, J. R.; Hair, M. L. *J. Phys. Chem.* **1978**, *82*, 1397−1399.

(42) Jiang, H.; Zhu, Y.; Feng, Q.; Su, Y.; Yang, X.; Li, C. *Chem. - Eur. J.* **2014**, *20*, 3106−3112.

(43) Guo, Z.; Liu, H.; Jiang, C.; Zhu, Y.; Wan, M.; Dai, L.; Jiang, L. *Small* **2014**, *10*, 2087−2095.
(44) Sheng, H.; Ji, H.; Ma, W.; Chen, C.; Zhao, J. *Angew. Chem., Int. Ed.* **2013**, *52*, 9686−9690.
(45) Lin, L.; Zhu, Q.; Xu, A. *J. Am. Chem. Soc.* **2014**, *136*, 11027−11033.
(46) Liu, Y.; Liu, H.; Wang, C.; Hou, S.-X.; Yang, N. *Environ. Sci. Technol.* **2013**, *47*, 13889−13895.
(47) Li, S.; Wu, D.; Liang, H.; Wang, J.; Zhuang, X.; Mai, Y.; Su, S.; Feng, X. *ChemSusChem* **2014**, *7*, 3002−3006.
(48) Sun, B.; Ou, Z.; Meng, D.; Fang, Y.; Song, Y.; Zhu, W.; Solntsev, P. V.; Nemykin, V. N.; Kadish, K. M. *Inorg. Chem.* **2014**, *53*, 8600−8609.
(49) Zheng, Y.; Jiao, Y.; Chen, J.; Liu, J.; Liang, J.; Du, A.; Zhang, W.; Zhu, Z.; Smith, S. C.; Jaroniec, M.; Lu, C. Q.; Qiao, S. Z. *J. Am. Chem. Soc.* **2011**, *133*, 20116−20119.
(50) Sheng, J.; Li, X.; Xu, Y. *ACS Catal.* **2014**, *4*, 732−737.
(51) Di, Y.; Wang, X.; Thomas, A.; Antonietti, M. *ChemCatChem* **2010**, *2*, 834−838.
(52) Zhao, L.; Bacsik, Z.; Hedin, N.; Wei, W.; Sun, Y.; Antonietti, M.; Titirici, M.-M. *ChemSusChem* **2010**, *3*, 840−845.
(53) Sugano, Y.; Shiraishi, Y.; Tsukamoto, D.; Ichikawa, S.; Tanaka, S.; Hirai, T. *Angew. Chem., Int. Ed.* **2013**, *52*, 5295−5299.
(54) Shiraishi, Y.; Sugano, Y.; Tanaka, S.; Hirai, T. *Angew. Chem., Int. Ed.* **2010**, *49*, 1656−1660.
(55) Shiraishi, Y.; Sugano, Y.; Ichikawa, S.; Hirai, T. *Catal. Sci. Technol.* **2012**, *2*, 400−405.
(56) Tsukamoto, D.; Shiraishi, Y.; Sugano, Y.; Ichikawa, S.; Tanaka, S.; Hirai, T. *J. Am. Chem. Soc.* **2012**, *134*, 6309−6315.
(57) Shiraishi, Y.; Tanaka, K.; Shirakawa, E.; Sugano, Y.; Ichikawa, S.; Tanaka, S.; Hirai, T. *Angew. Chem., Int. Ed.* **2013**, *52*, 8304−8308.